PCCP

ROYAL SOCIETY OF CHEMISTRY

PAPER

View Article Online
View Journal | View Issue

Check for updates

Cite this: Phys. Chem. Chem. Phys., 2025, **27**, 10387

Peroxymonosulfate activated M-MOF-74 (M = Co, Fe, Ni) visible light photocatalysts for methylene blue degradation enhancement†

Jiaqi Li,[ab] Yidan Zhang,[d] Pingyu Luo,[d] Chun Li,[a] Fanming Zeng,*[ab] Tiantian Sun,*[c] Hanhui Lei,[e] Xiaoteng Liu*[e] and Chunbo Liu[c]

Received 11th February 2025,
Accepted 11th April 2025

DOI: 10.1039/d5cp00544b

rsc.li/pccp

Persulphate-based advanced oxidation technology efficiently and cost-effectively removes organic dyes from water but designing stable photocatalytic systems and understanding their reaction mechanisms remain key challenges. Metal–organic frameworks (MOFs) have attracted considerable research attention for degrading organic pollutants owing to their high porosity, tunable structure, and ease of modification. In this study, a series of M-MOF-74 (M = Co, Fe, Ni) photocatalysts are synthesized by a hydrothermal method for methylene blue (MB) degradation. Among them, the Co-MOF-74 photocatalytic synergetic peroxymonosulfate system exhibits high catalytic activity after 30 min of visible light irradiation. MB degradation efficiency reaches 94.8%, and the reaction rate constant is 0.210 min^{-1}, which is approximately 19.44 times higher than the reaction rate constant of the original Co-MOF-74. Compared with Fe-MOF-74 and Ni-MOF-74, Co-MOF-74 exhibits better photocatalytic performance due to the dynamic changes in the valence state of cobalt, which more effectively facilitate the activation of PMS. In addition, this study analyses the possible degradation pathways of MB in water and toxicological evaluations of intermediate products, providing new insights for the effective removal of dyes in water.

1. Introduction

The rapid development of industrialization has led to the widespread use of organic dyes in industries such as textile, leather, and plastic industries. Methylene blue (MB), a stable organic cationic dye, is commonly used in the printing and dyeing industries. The direct discharge of MB into the environment not only causes severe pollution but also poses notable risks to aquatic organisms and human health.[1–4] Currently, effective dye wastewater treatment methods include physical adsorption, enhanced coagulation, photocatalytic oxidation and microbial electrochemical degradation.[5–8] However, numerous dyes exhibit excellent water solubility, leading to poor flocculation, adsorption, and biological treatment effects on dye-contaminated wastewater.[9,10] Therefore, an efficient, cost-effective and green method must be urgently developed to treat organic pollutants.

Advanced oxidation technology based on persulfate can generate various free radicals ($SO_4^{\bullet-}$, $^{\bullet}OH$ and $^{\bullet}O_2^{-}$) and non-free radicals ($^1O_2$), offering advantages such as high degradation efficiency and mild conditions, making the technology highly efficient for organic pollutant removal.[11–16] Several studies have demonstrated that peroxymonosulfate (PMS) can be activated by transition metals (*e.g.*, Co, Fe, Ni and Cu) to produce additional sulfate radicals. However, transition metals are prone to loss or deactivation during the reaction process, resulting in reduced catalytic activity.[17–21] Metal–organic frameworks (MOFs) can provide an ideal platform for the immobilization and dispersion of transition metals because they have an ordered pore structure and multiple metal active sites, which improve their catalytic activity. In addition, the framework structure of MOFs can protect transition metals, thereby mitigating their loss or deactivation during reactions.[22–26] Nevertheless, the design and synthesis of new, efficient, stable, and multifunctional MOF catalysts remains challenging. Moreover, to avoid secondary pollution, the reuse of MOF catalysts is essential for the effective treatment of environmental pollutants. Among numerous MOF materials, MOF-74 possesses

---

[a] *School of Materials Science and Engineering, Collaborative Innovation Center of Optical Materials and Chemistry, Changchun University of Science and Technology, Changchun 130022, China. E-mail: zengfm@126.com*

[b] *Collaborative Innovation Center of Optical Materials and Chemistry, Changchun University of Science and Technology, Changchun 130022, China*

[c] *Jilin Joint Technology Innovation Laboratory of Developing and Utilizing Materials of Reducing Pollution and Carbon Emissions, College of Engineering & College of Chemistry, Jilin Normal University, 136000, China. E-mail: stt@jlnu.edu.cn*

[d] *College of Chemistry, Jilin Normal University, 136000, China*

[e] *Department of Mechanical and Construction Engineering Faculty of Engineering and Environment, Northumbria University at Newcastle, Newcastle upon Tyne NE1 8ST, UK. E-mail: terence.liu@northumbria.ac.uk*

† Electronic supplementary information (ESI) available. See DOI: **https://doi.org/10.1039/d5cp00544b**

a core–shell structure, enabling it to absorb a broad spectrum of light, which is particularly important in the photocatalytic degradation process as it allows for more efficient utilization of sunlight and enhances photocatalytic efficiency. Additionally, it has a high pore volume and excellent stability, especially in low-temperature and aqueous environments, which facilitates its application in photocatalytic degradation under complex conditions.

In this study, a series of MOF catalysts (M-MOF-74, where M = Co, Fe, and Ni) are prepared and their MB degradation properties in a photocatalytic synergistic PMS system are investigated. The Co-MOF-74 photocatalytic synergetic PMS system (Co-MOF-74/PMS) exhibits better photocatalytic activity than Fe-MOF-74/PMS and Ni-MOF-74/PMS, effectively removing 94.8% of MB in water within 30 min, with a reaction rate constant of 0.210 min^{-1}. In this process, the metal ions of M-MOF-74 effectively enhanced the activation of PMS, generating various free radicals that considerably improved the MB degradation efficiency in water. However, different metals exhibit varying PMS activation abilities (Co > Fe > Ni). In addition, Co-MOF-74 shows a flower-like morphology composed of nanorods with a specific surface area of 434.873 $\text{m}^2\ \text{g}^{-1}$; this structure facilitated surface reactions of the reactants and rapid electron transmission. This study provides a reference value for designing high-performance photocatalysts for organic dye-contaminated wastewater treatment.

2. Experimental section

2.1. Materials

N,*N*-Dimethylformamide (DMF), 2,5-dihydroxyterephthalic acid (H_4DOBDC), cobalt nitrate hexahydrate ($Co(NO_3)_2\cdot 6H_2O$), iron chloride hexahydrate ($FeCl_3\cdot 6H_2O$), nickel nitrate hexahydrate ($Ni(NO_3)_2\cdot 6H_2O$) and perfluorosulfonic acid resin (Nafion) were obtained from Anaiji (Shanghai, China). MB, anhydrous ethanol, methanol (MeOH) and PMS were sourced from Aladdin (Shanghai, China). Isopropanol (IPA; ≥99.9% purity), disodium ethylenediaminetetraacetic acid (EDTA-2Na; 99% purity), and *p*-benzoquinone (PBQ; 99% purity) were supplied by McLean Biochemical Co., Ltd (Shanghai, China). Silver nitrate ($AgNO_3$), furfuryl alcohol (FFA) and anhydrous sodium sulfate (Na_2SO_4; ≥99% purity) were procured from China National Pharmaceutical Chemical Reagent Co., Ltd (Shanghai, China).

2.2. Preparation of M-MOF-74

H_4DOBDC (0.24 mmol) and $Co(NO_3)_2\cdot 6H_2O$ (0.72 mmol) were dissolved in 15 mL of a mixed solvent (DMF : ethanol : deionized water = 1 : 1 : 1). The resultant solution was ultrasonicated for 30 min and then transferred to a reaction kettle placed in a vacuum drying oven at 100 °C for 24 h. After the reaction was completed, the orange product was collected *via* centrifugation (7000 rpm, 3 min) and washed several times with DMF and MeOH. Then, the precipitate was dried under vacuum at 70 °C for 6 hours and the obtained product was named Co-MOF-74. The synthesis of Ni-MOF-74 followed the same procedure as that of Co-MOF, substituting $Ni(NO_3)_2\cdot 6H_2O$ instead of $Co(NO_3)_2\cdot 6H_2O$.

$FeCl_3\cdot 6H_2O$ (0.40 mmol) and H_4DOBDC (0.20 mmol) were dissolved in a mixed solution of 10 mL DMF, 1.5 mL 2-propanol, and 1.5 mL deionized water. The solution was ultrasonicated for 30 min before being transferred to a reaction kettle placed in an oven at 120 °C for 24 h. After cooling the reaction kettle, the product was collected *via* centrifugation (8000 rpm, 5 min) and washed several times with DMF, MeOH and deionized water. The final product (Fe-MOF-74) was obtained by vacuum drying at 100 °C for 10 h. The synthetic route of M-MOF-74 is shown in Scheme 1.

2.3. Characterization, photocatalytic activity, and photoelectrochemical measurements

Detailed information on the characterization, photocatalytic activity, and photoelectrochemical measurements of this work can be obtained from the ESI.†

3. Results and discussion

3.1. Structural and morphological characteristics

The crystal structure of M-MOF-74 catalysts is investigated by X-ray diffraction (XRD). As shown in Fig. 1a, the diffraction peaks of Co-MOF-74, Fe-MOF-74 and Ni-MOF-74 at 6.8°, 18.2°, 21.9°, 25.0°, 34.3° and 35.9° correspond to the (100), (019), (004), (008), (002) and (001) crystal planes of MOF-74, respectively. These peaks are completely consistent with their simulated diffraction

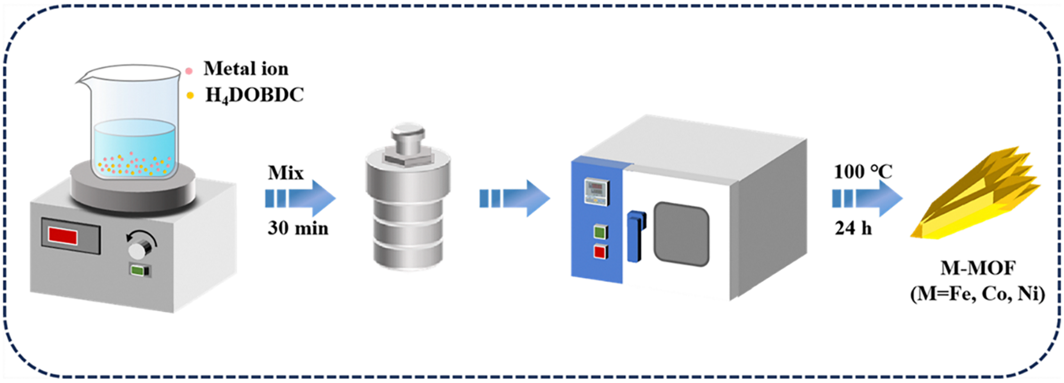

Scheme 1 Preparation method of M-MOF (M = Co, Fe, Ni).

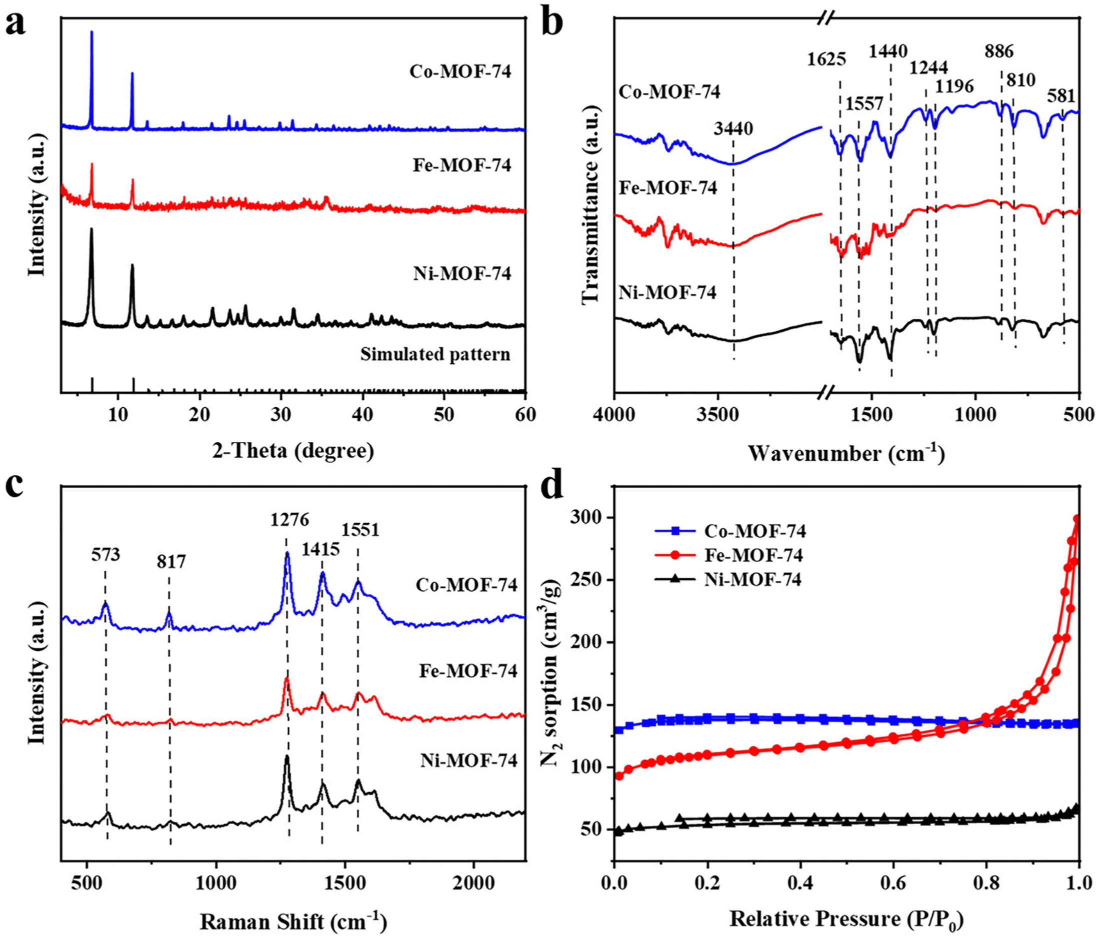

Fig. 1 XRD patterns (a), FT-IR spectra (b), Raman spectra (c) and N_2 adsorption–desorption curves (d) of Co-MOF-74, Fe-MOF-74 and Ni-MOF-74.

patterns and no obvious impurity peaks are observed.[27,28] Thus, it is confirmed that the M-MOF-74 catalysts are successfully synthesized.

The structural properties of M-MOF-74 catalysts are further analyzed through Fourier transform infrared (FTIR) spectroscopy (Fig. 1b). The broad peak at 3440 cm^{-1} indicates the presence of hydroxyl groups from water. The two peaks at 1625 and 1556 cm^{-1} are attributed to the stretching vibrations of C=O, while the peak at 1440 cm^{-1} corresponds to the C=C bonds within the benzene ring. The peak at 1244 cm^{-1} is attributed to the stretching vibration of the C–O bond in the carboxyl group. In addition, the peak at 1196 cm^{-1} is attributed to the C–H bending vibration in the benzene ring, and the peak at 1125 cm^{-1} corresponds to the stretching vibration of the C–O bond within the benzene ring skeleton. The peaks at 886 and 810 cm^{-1} represent the bending vibration peak of the C–H bond outside the benzene ring and the bending vibration of the benzene ring itself, respectively. The stretching vibration of the metal–oxygen (M–O) bond at 581 cm^{-1} aligns with the previously reported FTIR spectrum of MOF-74.[29,30]

Fig. 1c shows the Raman spectrum of M-MOF-74 catalysts. The characteristic peak at 573 cm^{-1} corresponds to the bending vibration of the M–O bond, indicating the coordination of Co, Fe or Ni with O in the MOF-74 structure. The peak at 817 cm^{-1} is attributed to the bending vibration of the C–H bond, which is a characteristic of the benzene ring structure in MOF-74. This vibration mode indicates a relatively stable binding state between the ligand and the metal center. The peaks at 1276 cm^{-1}, 1551 cm^{-1} and 1700 cm^{-1} are typically associated with the stretching vibrations of carboxyl or carbonyl groups. The peaks at 1415 cm^{-1} and 1500 cm^{-1} correspond to the stretching vibration of the C=C bond, reflecting the conjugated benzene ring structure.[31] These results are consistent with the FTIR spectra, further confirming the successful synthesis of M-MOF-74 catalysts.

The N_2 adsorption–desorption isotherms of the catalysts are recorded and the specific surface areas and pore size distributions are calculated through the Brunauer–Emmett–Teller equation. As shown in Fig. 1d, the N_2 adsorption–desorption isotherms of Co-MOF-74, Fe-MOF-74 and Ni-MOF-74 exhibit type IV isotherms with H3 hysteresis. The isotherms exhibit an upward trend as the relative pressure (P/P_0) exceeds 0.8, suggesting the presence of mesopores in the samples. The pore diameters of Co-MOF-74, Fe-MOF-74 and Ni-MOF-74 are primarily concentrated between 2 and 10 nm, which is a typical characteristic of mesoporous materials (Fig. S1, ESI†). The specific surface areas of Co-MOF-74, Fe-MOF-74 and Ni-MOF-74 are 434.873, 354.477 and 165.477 $m^2\ g^{-1}$, respectively (Table S1, ESI†). Among them, the specific surface area of Co-MOF-74

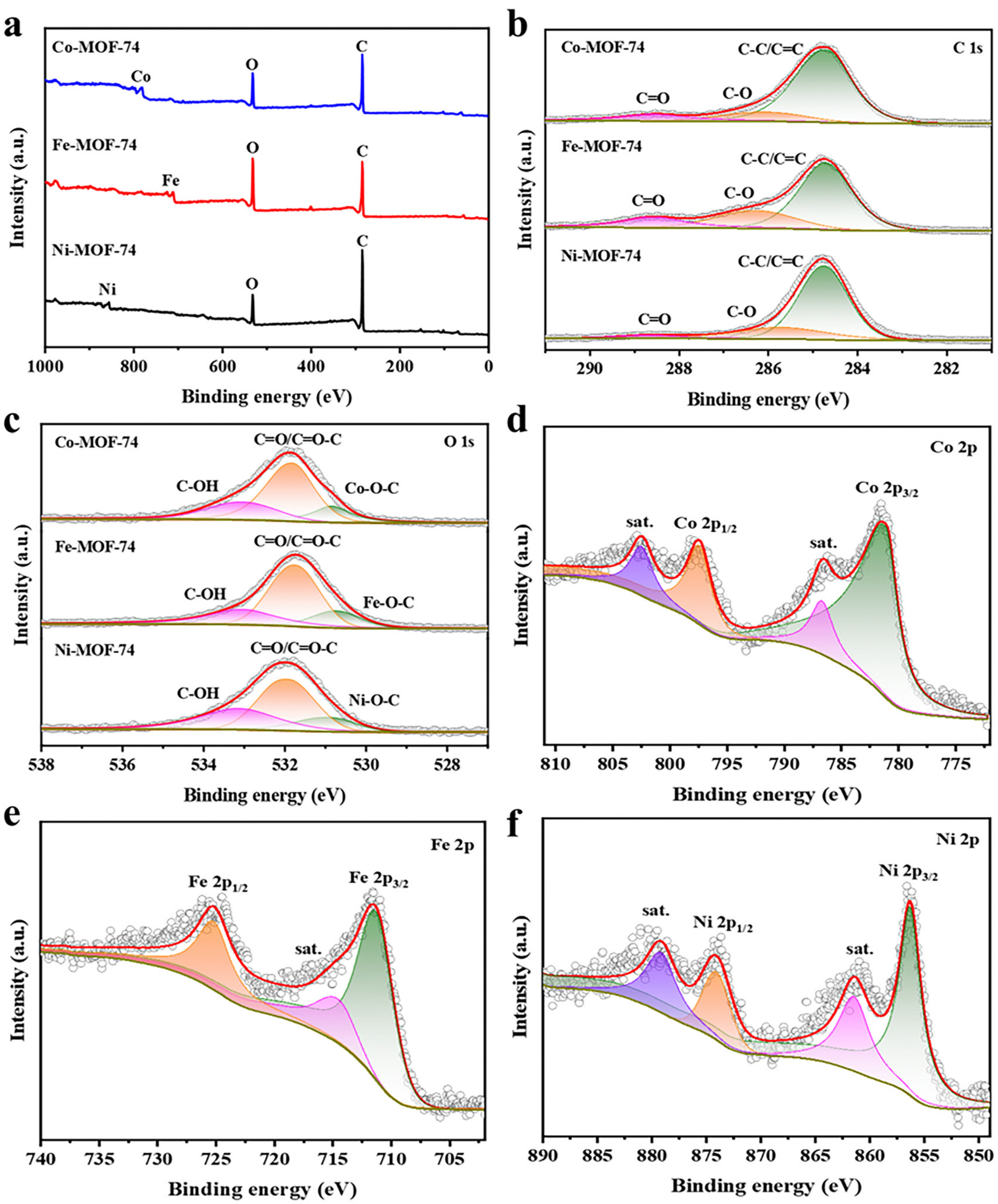

Fig. 2 XPS survey spectra (a), C 1s spectra (b) and O 1s (c) spectra of Co-MOF-74, Fe-MOF-74 and Ni-MOF-74. Co 2p spectra of Co-MOF-74 (d). Fe 2p spectra of Fe-MOF-74 (e). Ni 2p spectra of Ni-MOF-74 (f).

is considerably higher, which can provide more active sites for photocatalytic degradation of pollutants, potentially improving its photocatalytic degradation performance.

The surface chemical compositions of Co-MOF-74, Fe-MOF-74 and Ni-MOF-74 are analyzed using X-ray photoelectron spectroscopy (XPS). Fig. 2a shows the XPS survey spectra of Co-MOF-74, Fe-MOF-74 and Ni-MOF-74. The characteristic peaks with binding energies of 285.08, 532.08, 781.71, 711.15 and 856.17 eV correspond to C 1s, O 1s, Co 2p, Fe 2p and Ni 2p, respectively. Fig. 2b displays the C 1s high-resolution spectrum with three characteristic peaks at 284.80, 286.23 and 288.53 eV, which are attributed to the C–C/C═C, C–O and C═O, respectively. Fig. 2c shows the O 1s X-ray photoelectron spectrum. The peaks at 531.83 and 533.18 eV are assigned to C═O/C═O–C and C–OH, respectively, while the characteristic peak at 530.83 eV corresponds to M–O–C (M = Co, Fe, Ni). For the Co 2p spectrum of Co-MOF-74, four characteristic peaks were obtained by fitting. The peaks at 781.53 and 797.48 eV correspond to Co^{3+}, respectively, and the peaks at 786.78 and 802.58 eV correspond to Co^{2+} (Fig. 2d).[32,33] Four peaks were identified in the fine spectral fitting of Fe 2p in Fe-MOF-74. The peaks at 711.53 eV and 725.43 eV are attributed to Fe^{3+}. The peaks at

714.98 eV and 726.83 eV correspond to Fe^{2+} (Fig. 2e).[34] Similarly, the peaks at 856.28 and 874.18 eV are attributed to Ni^{3+}, while the peaks at 861.38 and 879.63 eV correspond to Ni^{2+} (Fig. 2f).[35] These results confirm the successful synthesis of M-MOF-74 catalysts.

The morphology of M-MOF-74 catalysts is observed by scanning electron microscopy (SEM). The morphological characteristics of Co-MOF-74 are shown in Fig. 3a. Co-MOF-74 exhibits a flower-like structure with a smooth surface and a length of approximately 30–32 μm. As shown in Fig. 3b, Co, O and C are evenly distributed within the Co-MOF-74 structure. Combined with the XRD patterns, the Co ions uniformly participate in the coordination of the framework structure, forming a single metal-coordinated MOF material. Fig. 3c shows a SEM image of Fe-MOF-74, which displays a uniform polyhedral prism with a size of approximately 10–12 μm. The elemental mapping image (Fig. 3d) shows that Fe, O, and C are evenly distributed in Fe-MOF-74, with no impurity peaks from unrelated elements, indicating high sample purity. Fig. 3e shows that Ni-MOF-74 consists of several stacked nanoshuttle structures with uneven particle sizes and an irregular block structure. The elemental mapping image of Ni-MOF-74 shows that Ni, O, and C are evenly distributed (Fig. 3f).

3.2. Evaluation of catalytic performance toward PMS activation

The photocatalytic degradation performance of different materials on MB in aqueous solution is analyzed. Fig. 4a shows the MB degradation efficiencies of Co-MOF-74/PMS, Fe-MOF-74/PMS, Ni-MOF-74/PMS, PMS and Co-MOF-74. After stirring in the dark for 40 min, the samples reach adsorption–desorption equilibrium. Then, an appropriate amount of PMS is added to the reaction system and the light turned on for photocatalytic degradation experiments. The results demonstrate that Fe-MOF-74/PMS and Ni-MOF-74/PMS exhibit poor MB degradation effects, with Fe-MOF-74/PMS (73.7%) outperforming Ni-MOF-74/PMS (63.4%). The Co-MOF-74/PMS exhibits the best catalytic activity, removing 94.8% of MB in water within 30 min. In addition, the MB degradation effect of pure PMS is evaluated. The results show that the MB removal efficiency of pure PMS is

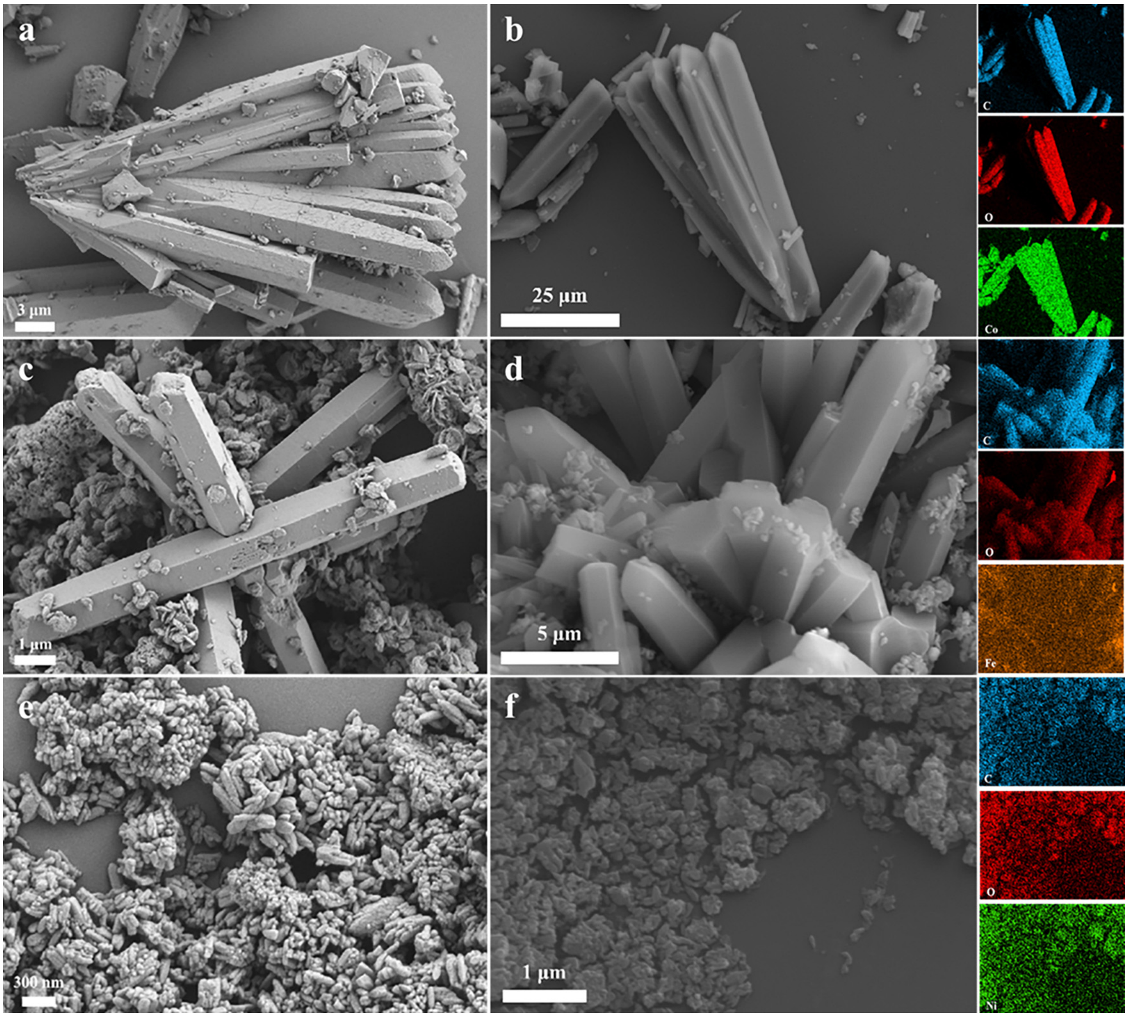

Fig. 3 SEM image (a) and elemental mapping images (b) of Co-MOF-74. SEM image (c) and elemental mapping images (d) of Fe-MOF-74. SEM image (e) and elemental mapping images (f) of Ni-MOF-74.

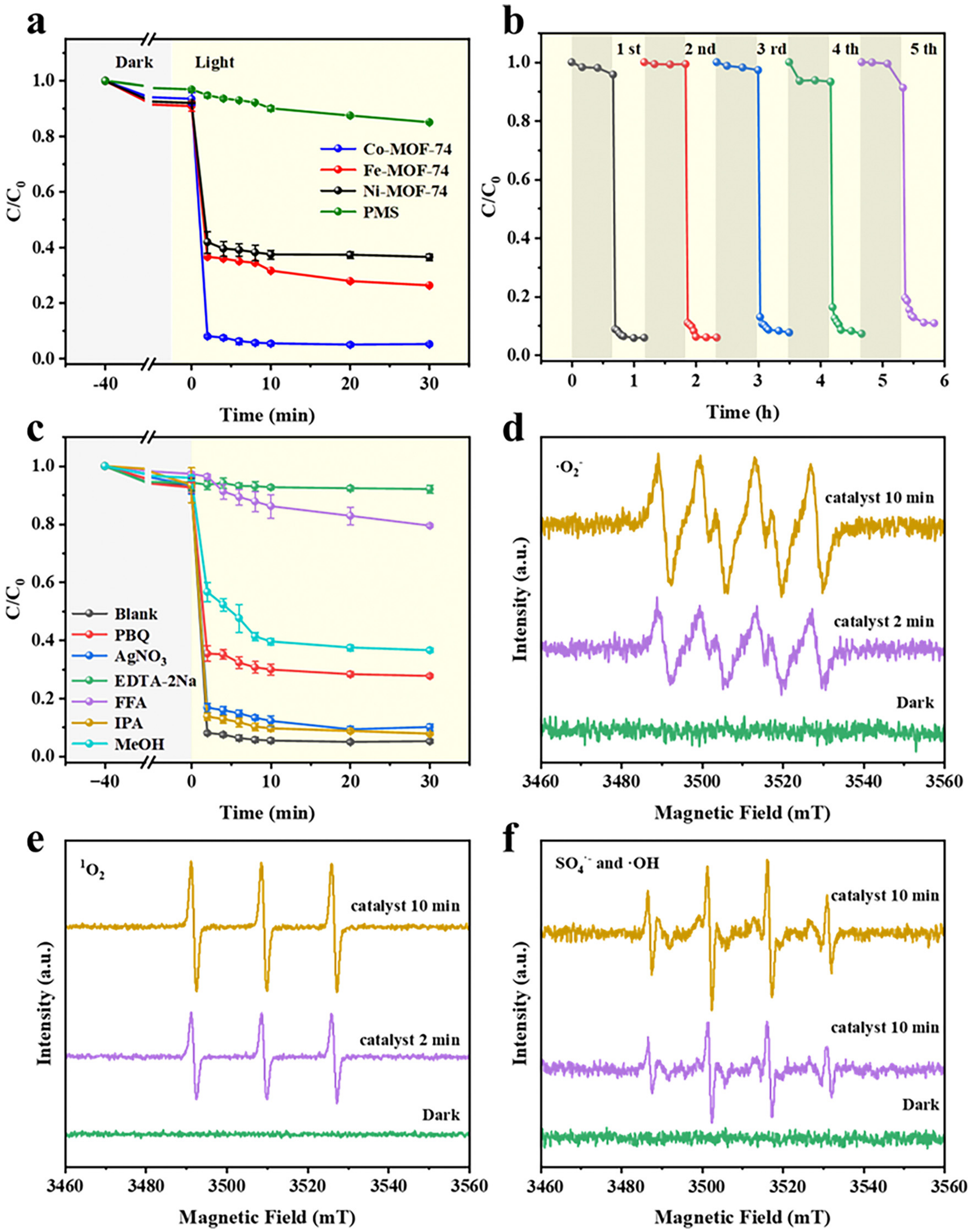

Fig. 4 The degradation efficiency of MB by Co-MOF-74/PMS, Fe-MOF-74/PMS, Ni-MOF-74/PMS, PMS and Co-MOF-74 (a). The stability of Co-MOF-74/PMS in degrading MB (b). The effects of different scavengers on MB degradation (c). The ESR spectra of DMPO–$^{\bullet}O_2^-$ signals (d), TEMP–$^1O_2$ signals (e), DMPO–$^{\bullet}OH$ and DMPO–$SO_4^{\bullet -}$ signals (f) in the Co-MOF-74-catalyzed system.

only 14.9%, likely due to the small amount of reactive oxygen species (ROS) generated by PMS self-decomposition when exposed to visible light. Meanwhile, when only Co-MOF-74 is present in the system, the MB removal efficiency is 29.6%, which is obviously lower than that of Co-MOF-74/PMS. These results indicate that the combination of the synthesized catalyst system and PMS greatly enhances the MB degradation efficiency, indicating that the catalyst addition can activate PMS to varying degrees. The reaction rate constants for MB degradation activated by different catalyst samples are calculated by first-order kinetics (K_{app}) (Fig. S2, ESI†). The K_{app} value for Co-MOF-74/PMS is 0.210 min^{-1}, which is 2.69, 3.08, 32.30 and 19.44 times higher than those for Fe-MOF-74/PMS (0.078 min^{-1}), Ni-MOF-74/PMS (0.078 min^{-1}), PMS (0.0065 min^{-1}) and Co-MOF-74 (0.0108 min^{-1}), respectively.

The effects of different conditions on MB degradation by Co-MOF-74/PMS are investigated *via* a single-factor experiment. When the PMS concentration increases from 0.2 to 0.8 mmol L^{-1}, the MB degradation efficiency increases from 65.4% to 94.8% within 30 min. This phenomenon can be ascribed to the augmented concentration of PMS, which facilitates a higher propensity for $HSO_5^{\bullet-}$ to interact with the catalytic active sites on the catalyst surface. This interaction engenders a surfeit of radicals within the system, thereby potentiating the degradation efficiency. However, when the PMS concentration further increases to 1.0 mmol L^{-1}, the MB degradation efficiency shows a minimal change. This may be because when the PMS concentration increases to a certain level, the generation of active species may reach saturation (Fig. S3a, ESI†).

The experimental results show that the MB degradation efficiency increases with the catalyst dosage from 0.1 to 0.4 g L^{-1}, with 0.4 g L^{-1} being the optimal dosage (Fig. S3b, ESI†). This improvement is due to the increased number of catalytic active sites during the reaction, which enhances the PMS activation rate in the system, thus increasing the MB oxidation degradation rate. However, upon further increasing the Co-MOF-74 dosage to 0.5 g L^{-1}, no improvement in the MB degradation effect is observed. This may be because at higher concentrations, the free radicals generated by the excessive catalyst tend to collide with each other and undergo quenching, reducing the actual number of free radicals available to participate in the degradation reaction, which ultimately lowers the effectiveness of Co-MOF-74/PMS in degrading MB in water.

Next, the influence of different pH values on MB degradation was investigated (Fig. S3c, ESI†). The MB degradation efficiencies are 76.0%, 91.6%, 94.8%, 84.6% and 80.8% at pH values of 3.11, 5.26, 7.08, 9.14 and 11.21, respectively. The results indicate that the addition of Co-MOF-74 facilitates MB photodegradation under neutral conditions, whereas the degradation efficiency is inhibited under strong acidic or alkaline conditions. To further understand the interaction between Co-MOF-74 and MB under different pH conditions, we performed zeta potential analysis to assess the charge state of Co-MOF-74 in various pH solutions (Fig. S4, ESI†). According to the literature, when $pH < 7$, MB exists as MBH^{2+} in solution; and when $pH > 7$, MB is the predominant form. As the pH of the solution increases from 3.33 to 11.21, the zeta potential of Co-MOF-74 decreases. When $pH < 4.5$, Co-MOF-74 carries a positive charge, which repels MBH^{2+} and inhibits MB adsorption to the complex, resulting in lower degradation. When $pH > 4.5$, the Co-MOF-74 complex surface carries a negative charge, creating electrostatic attraction with MBH^{2+}, which promotes complex adsorption to MB, thereby considerably enhancing the MB degradation efficiency. When $pH > 7$, MB is neutral and does not strongly interact with the negatively charged complex surface of Co-MOF-74, thereby decreasing the degradation efficiency.

To explore the feasibility of Co-MOF-74 for degrading MB under complex water quality conditions, various inorganic ions (Cl^-, HCO_3^- and $H_2PO_4^-$) and humic acid (HA) are added to the reaction system. As shown in Fig. S3d (ESI†), the addition of Cl^- shows a negligible MB degradation effect. However, the addition of HCO_3^- and $H_2PO_4^-$ considerably inhibits the ability of Co-MOF-74/PMS to activate PMS for MB photocatalytic degradation. The inhibition of HCO_3^- occurs because it acts as an effective scavenger for radicals and oxidants, quenching $SO_4^{\bullet-}$ and generating less active $CO_3^{\bullet-}$ and HSO_5^- is further converted by HCO_3^- into the nonoxidizing HCO_4^-. In the case of $H_2PO_4^-$, it not only scavenges $SO_4^{\bullet-}$ radicals but also chelates with active sites on the catalyst surface or hydroxyl groups, thereby decreasing the MB degradation efficiency. Meanwhile, HA, a common natural organic substance found in water, contains carboxyl and hydroxyl groups that can interact with the active centers of the catalyst, competing for adsorption sites and ROS with MB. The experimental results show that when a certain amount of HA is added to the system, the MB degradation efficiency decreases to 84.2%. Therefore, HA exhibits a strong inhibitory effect on the MB degradation reaction.

We conducted cyclic degradation experiments based on Co-MOF-74/PMS to evaluate the long-term operational performance of Co-MOF-74. As shown in Fig. 4b, the degradation efficiency of MB only slightly decreased after five cycles, which can be attributed to the adsorption of MB on the surface of Co-MOF-74 or its degradation products. These products weaken the complexation between PMS and Co-MOF-74 as well as the activation effect of PMS. In addition, the stability of Co-MOF-74 is investigated by XRD, FTIR and XPS. According to the XRD and FTIR spectra (Fig. S5, ESI†), no notable changes are observed in the positions of the diffraction peaks corresponding to Co-MOF-74 in the samples before and after the reaction, indicating that the photocatalytic reaction does not influence the main Co-MOF-74 structure. The XPS results of the catalyst before and after the reaction also confirm the chemical structural stability of Co-MOF-74. As shown in Fig. S6a–d (ESI†), compared with Co-MOF-74 before the reaction, no notable changes are observed in the characteristic peaks of C 1s, O 1s, and Co 2p after the reaction, indicating that the photocatalytic reaction does not influence the chemical bonding structure of Co-MOF-74. These results indicate that Co-MOF-74 exhibits high catalytic activity in activating PMS for the photocatalytic oxidation of organic pollutants in water, while also demonstrating good stability.

To compare the mineralization capabilities of the M-MOF-74 catalysts on MB, TOC tests are performed on the solutions after photocatalytic degradation (Fig. S7, ESI†). Co-MOF-74 exhibits higher mineralization efficiency than Fe-MOF-74 (31.24%) and Ni-MOF-74 (24.46%). However, its mineralization effect also did not reach a very high level, with only 42.16% of MB being completely mineralized and converted to CO_2 and H_2O. The low mineralization efficiency indicates that most MB molecules underwent incomplete degradation, resulting in the generation of competitive intermediate products.

The campus lake water (Jilin Normal University, Siping, China) and tap water from a laboratory (Jilin Normal University, Siping, China) are selected to test the applicability of Co-MOF-

74 in real water samples (Fig. S8, ESI†). The experimental results demonstrate that the MB removal rates in both water groups are almost identical to those in the deionized water group. This observation suggests that the photocatalytic performance of Co-MOF-74 is minimally influenced by real environmental conditions, highlighting its great potential for application in the photocatalytic degradation of MB in natural water bodies. In addition, PMS, a sulfur-containing oxidant, may release SO_4^{2-} into the environment. In this study, the PMS dosage used is only 0.8 mmol L^{-1}, which, if fully converted to SO_4^{2-} would yield a concentration of 76.8 mg L^{-1}—far below China's drinking water quality sanitation standard (250 mg L^{-1}). Therefore, it can be considered a safe means for actual water treatment.

Quenching experiments are conducted to explore the active species of Co-MOF-74/PMS involved in MB degradation. The experimental results show (Fig. 4c) that Co-MOF-74/PMS can degrade 94.8% of MB within 30 min without any quencher. The addition of EDTA-2Na to the reaction system severely inhibits the MB removal efficiency, indicating that h^+ plays a pivotal role in the catalytic system. Furthermore, the addition of PBQ decreases the MB degradation efficiency to 72.4%, suggesting that the superoxide radicals contribute to the MB degradation by Co-MOF-74/PMS. Notably, $^\bullet O_2^-$ is less influenced by inorganic ions and HA in natural water bodies, which suggests that Co-MOF-74/PMS exhibits good degradation performance in real water treatment. IPA and MeOH were used to quench $^\bullet OH$ and $SO_4^{\bullet-}$, respectively. In the presence of IPA, the MB degradation efficiency remains almost unchanged, indicating that $^\bullet OH$ plays a minor role in the photocatalytic degradation. However, when MeOH is added to the system, the MB removal efficiency decreases to 63.5%, highlighting the stronger influence of $SO_4^{\bullet-}$ compared to $^\bullet OH$. Finally, FFA was used to quench the singlet oxygen ($^1O_2$). The addition of FFA greatly inhibits MB degradation by Co-MOF-74/PMS, with the efficiency dropping to 20.6%, indicating that $^1O_2$ is the main active radical in Co-MOF-74/PMS. Therefore, radical capture experiments suggest that h^+, $^\bullet O_2^-$, $SO_4^{\bullet-}$ and $^1O_2$ are the primary active species in Co-MOF-74/PMS, collectively contributing to the effective MB removal. To further confirm the presence of radicals in the system, we conducted ESR tests and observed the corresponding DMPO–$^\bullet O_2^-$, DMPO–$^\bullet OH$, DMPO–$SO_4^{\bullet-}$ and TEMP–$^1O_2$ adduct signals after the induction of the trapping agent reactions (Fig. 4d–f). For Co-MOF-74/PMS, no ESR signals of the active substances are observed in the dark state; however, upon illumination, DMPO–$^\bullet O_2^-$, DMPO–$^\bullet OH$, DMPO–$SO_4^{\bullet-}$ and TEMP–$^1O_2$ adduct signals appear, and their peak intensity increase continuously with the reaction time. These results confirm that Co-MOF-74 activates PMS to generate ROS under light irradiation. In summary, Co-MOF-74/PMS involves the coupling of both the radical and non-radical species, with h^+, $^\bullet O_2^-$, $SO_4^{\bullet-}$ and $^1O_2$ playing pivotal roles.

3.3. Photocatalytic degradation pathways and toxicity analysis of MB

This study employed liquid chromatography-mass spectrometry (LC-MS) to identify intermediate products formed during the MB degradation process (Fig. 5a and Fig. S9, ESI†). In pathway I, MB reacts continuously with ROS, breaking the double bond between S and C to form P1 (*m*/*z* = 286.4). Subsequently, P1

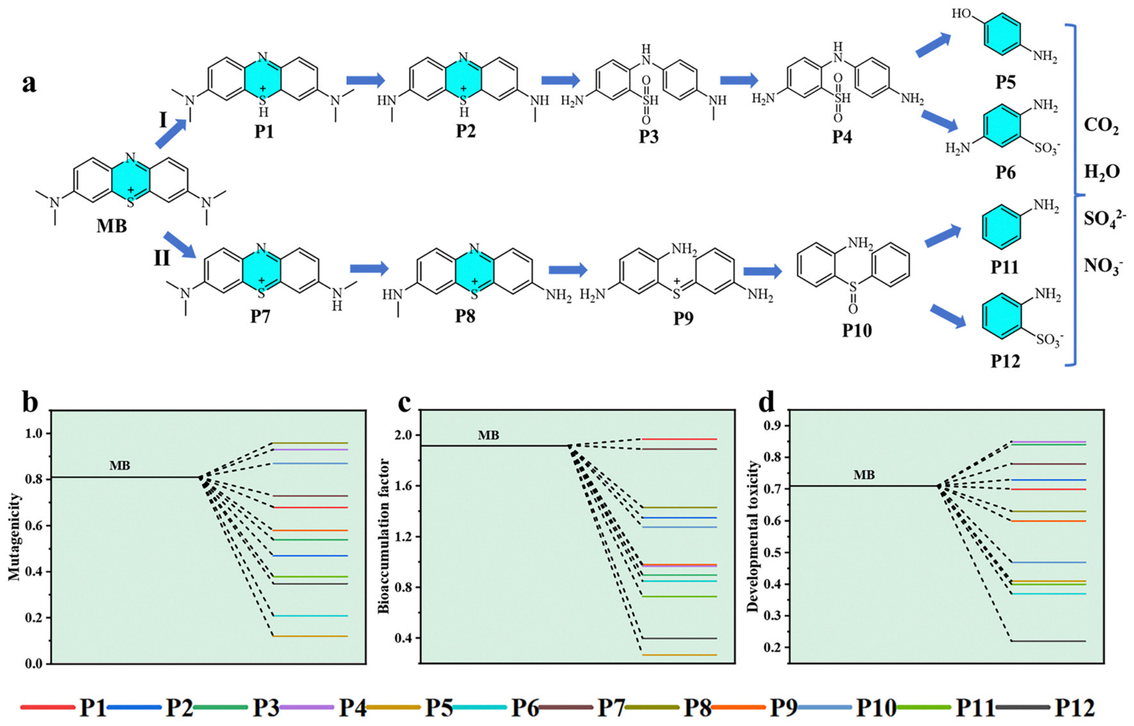

Fig. 5 The possible degradation pathways of MB by Co-MOF-74 (a), mutagenicity, bioaccumulation factor and developmental toxicity of MB degradation intermediates (b)–(d).

undergoes demethylation, resulting in the formation of P2 (m/z = 257.0). Next, P2 forms an S–O bond during the photocatalytic process, accompanied by the demethylation of the amino group, leading to the formation of P3 (m/z = 277.3) and P4 (m/z = 263.1). Further ROS attack causes the N–C bond of P4 to break, generating P5 (m/z = 186.7) and P6 (m/z = 109.3). In pathway II, MB undergoes gradual demethylation under the action of ROS to form P7 (m/z = 270.1) and P8 (m/z = 242.2). Subsequently, as P8 undergoes demethylation, its central aromatic heterocycle is attacked by ROS, forming P9 (m/z = 231.0). Immediately, ROS attacks the S double bond and the C–N bond, causing deacylation reactions on both sides of P9, resulting in the formation of P10 (m/z = 217.0). The S site of P10 is attacked, producing aniline (P11; m/z = 93.0) or 2-aminobenzenesulfonate (P12; m/z = 172.9).

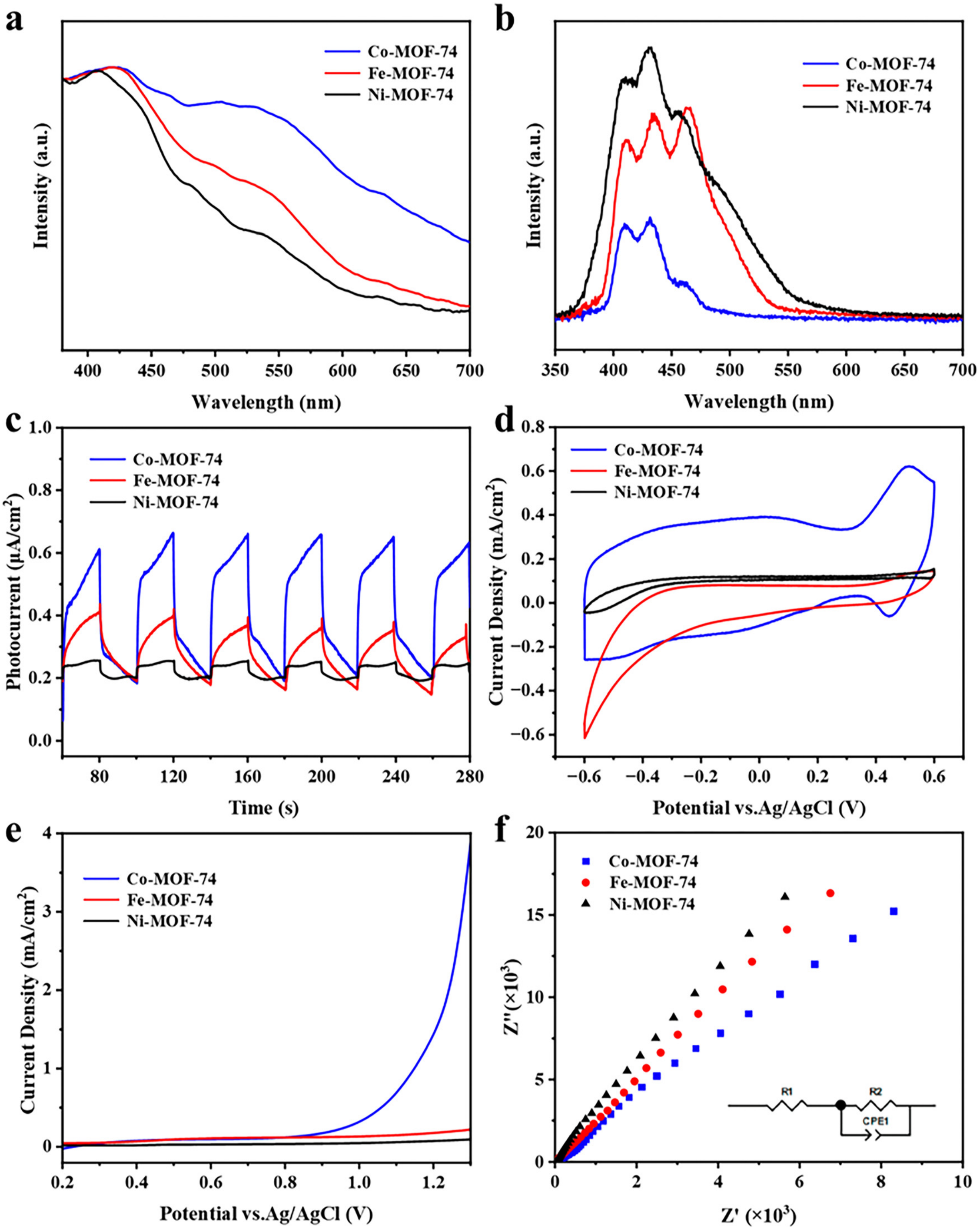

Fig. 6 UV-Vis DRS (a), PL (b), current–time plots (c), CV curves (d), LSV curves (e) and EIS results (f) of Co-MOF-74, Fe-MOF-74 and Ni-MOF-74.

Finally, under the synergistic action of ROS, the intermediates are further oxidized into small molecules, ultimately mineralizing into CO_2, H_2O, SO_4^{2-}, and NO_3^-.

The toxicity assessment software tool is used to predict the toxicity (mutagenicity, bioaccumulation factor, and developmental toxicity) of MB and its degradation intermediates. As shown in Fig. 5b, MB is mutagenically positive. With continuous photodegradation, most of the intermediates are oxidized to mutagenic negative substances, indicating that photodegradation considerably reduces its genotoxicity. Compared with the bioconcentration factor of MB, the bioconcentration factors of the degradation byproducts are markedly reduced, except for P1 (m/z = 286.4; Fig. 5c). Furthermore, Co-MOF-74/PMS effectively reduces the developmental toxicity indicators of most intermediate byproducts formed during MB degradation. As shown in Fig. 5d, the developmental toxicity of the intermediates (except for P2, P3, P4, and P7) is reduced, with P5, P6, P10, P11, and P12 identified as developmentally nontoxic substances. In summary, although the toxicity of some intermediate byproducts slightly increased, the overall toxicity remained within a safe range, with the toxicity of most intermediates reduced. Therefore, Co-MOF-74/PMS represents a "green" method with remarkable practical potential for treating MB-contaminated wastewater.

3.4. Photoelectrochemical test

The light absorption characteristics greatly influence the photocatalytic activity of materials. As shown in Fig. 6a, Co-MOF-74, Fe-MOF-74 and Ni-MOF-74 exhibit absorption ability in the visible light region. Among these MOF catalysts, Co-MOF-74 demonstrates the strongest light absorption ability, and its broadened light absorption band can photogenerate more electron–hole pairs, thereby improving its photocatalytic activity. The bandgaps of Co-MOF-74, Fe-MOF-74 and Ni-MOF-74, calculated using the Tauc equation from ultraviolet-visible DSR data, are 1.62, 1.82 and 1.90 eV, respectively (Fig. S10, ESI†). The steady-state fluorescence spectra of Co-MOF-74, Fe-MOF-74 and Ni-MOF-74 are recorded to investigate the migration and recombination of photogenerated electrons and holes. As shown in Fig. 6b, Co-MOF-74, Fe-MOF-74 and Ni-MOF-74 exhibit emission peaks at approximately 425 nm, with the fluorescence peak intensities following the order: Ni-MOF-74 > Fe-MOF-74 > Co-MOF-74. The fluorescence intensity of Co-MOF-74 is the lowest, indicating that its electron–hole recombination is suppressed, which accelerates the charge transfer rate and effectively improves its photocatalytic performance. Fig. 6c presents the photocurrent response curves of Co-MOF-74, Fe-MOF-74 and Ni-MOF-74. Upon light irradiation, the photocurrent immediately increases to its maximum value before reaching the steady state. When the light source is turned off, the photocurrent immediately decays to the initial state. The reproducibility of the photocurrent response of the sample during repeated optical switching indicates the stability of the sample under light irradiation. Notably, Co-MOF-74 exhibits a stronger photocurrent density signal than Fe-MOF-74 and Ni-MOF-74, indicating that Co-MOF-74 exhibits more efficient photogenerated electron–hole separation and higher photocatalytic activity. When delving into the electrochemical performance of these materials, we initially concentrated on the cyclic voltammetry (CV) profiles, which serve as a pivotal diagnostic tool for evaluating the electrochemical activity and redox behavior of materials. The CV curves of Co-MOF-74, Fe-MOF-74, and Ni-MOF-74, as depicted in Fig. 6d, reveal that Co-MOF-74 exhibited exceptional electrocatalytic activity, characterized by a markedly higher current density compared to Fe-MOF-74 and Ni-MOF-74. This pronounced current density is a direct indicator of Co-MOF-74's superior efficacy in facilitating redox reactions, thereby substantiating its potential utility in photocatalytic applications. Furthermore, to ascertain the electronic conductivity and charge transport properties of these materials, we employed linear sweep voltammetry (LSV). The LSV data presented in Fig. 6e indicate that Co-MOF-74 also exhibited a higher current density, signifying expedited electron transport kinetics within this material. This attribute is of paramount importance for efficient charge separation and transfer in photocatalytic processes, as rapid electron conduction mitigates charge recombination events and thereby enhances the overall photocatalytic efficiency. In the context of evaluating charge transfer efficiency, the Nyquist plot, a cornerstone of electrochemical impedance spectroscopy (EIS), provides invaluable insights. Typically, the efficiency of charge transfer is inferred from the radius of the semicircular arc in the Nyquist plot, which corresponds to the charge transfer resistance (R_{ct}). The Nyquist plot in Fig. 6f demonstrates that Co-MOF-74 possesses a smaller semicircle radius relative to Fe-MOF-74 and Ni-MOF-74, indicative of reduced R_{ct} and thereby enhanced charge transfer kinetics. This smaller R_{ct} is synonymous with higher charge transfer efficiency, further corroborating the exceptional performance of Co-MOF-74 in photoinduced charge separation mechanisms.

4. Conclusions

In this study, we successfully synthesized a series of MOF catalysts (M-MOF-74, M = Co, Fe, and Ni) using a hydrothermal method. Among the studied catalysts, Co-MOF-74 exhibited superior photocatalytic performance, achieving 94.8% of MB degradation efficiency within 30 min, with a K_{app} of 0.210 min^{-1}. The exceptional performance of the Co-MOF-74 photocatalyst can be attributed to its multiple active sites and large specific surface area. In addition, the presence of Co effectively enhanced PMS activation and MB degradation. Intermediate byproducts were identified during MB degradation, and their environmental toxicity was evaluated. The findings of this study provide a comprehensive understanding of photocatalytic PMS activation for dye degradation and highlight an effective strategy for synthesizing MOF materials with good photocatalytic performance.

Data availability

The data are available from the corresponding author upon reasonable request.

Conflicts of interest

The authors declare that they have no known competing financial interests or personal relationships that could have appeared to influence the work reported in this paper.

Acknowledgements

This work is supported by the Natural Science Foundation Project of Jilin Province (YDZJ202402054CXJD), the National Natural Science Foundation of China (No. 22478150) and the Government Funded Projects (627010104).

References

1 Z. Bao, N. Gao, N. Du, S. Luo and Y. Liu, A self-contained catalytic sponge for point-of-use solar driven persulfate oxidation and photothermal evaporation, *Chem. Eng. J.*, 2025, **503**, 158466.

2 X. Cheng, R. Guan, Z. Wu, Y. Sun, W. Che and Q. Shang, Establishing carrier transport channels based on Ti–S bonds and enhancing the photocatalytic performance of MXene quantum dots-$ZnIn_2S_4$ for ammonia synthesis, *InfoMat*, 2024, **6**, e12535.

3 W. Li, G. Liao, W. Duan, F. Gao, Y. Wang, R. Cui, X. Wang and C. Wang, Synergistically electronic interacted PVDF/CdS/TiO_2 organic-inorganic photocatalytic membrane for multi-field driven panel wastewater purification, *Appl. Catal., B*, 2024, **354**, 124108.

4 Z. Li, H. Xu, Y. Zheng, L. Liu, L. Li, Z. Lou and L. Wang, A reconfigurable heterostructure transistor array for monocular 3D parallax reconstruction, *Nat. Electron.*, 2025, **8**, 46.

5 M. Ahmadian and M. Jaymand, Interpenetrating polymer network hydrogels for removal of synthetic dyes: a comprehensive review, *Coord. Chem. Rev.*, 2023, **486**, 215152.

6 Z. Yousefzadeh, M. Montazer and A. Mianehro, Plasmonic photocatalytic nanocomposite of in-situ synthesized MnO_2 nanoparticles on cellulosic fabric with structural color, *Carbohydr. Polym.*, 2024, **326**, 121622.

7 A. Singh, D. Pal, A. Mohammad, A. Alhazmi, S. Haque, T. Yoon, N. Srivastava and V. Gupta, Biological remediation technologies for dyes and heavy metals in wastewater treatment: new insight, *Bioresour. Technol.*, 2022, **343**, 126154.

8 D. Patel, A. Singh, S. Ambati, R. Singh and R. Sonwani, An overview of recent advances in treatment of complex dye-containing wastewater and its techno-economic assessment, *J. Environ. Manage.*, 2024, **370**, 122804.

9 S. Sarkar, N. Ponce, A. Banerjee, R. Bandopadhyay, S. Rajendran and E. Lichtfouse, Green polymeric nanomaterials for the photocatalytic degradation of dyes: a review, *Environ. Chem. Lett.*, 2020, **18**, 1569.

10 K. Xie, J. Fang, L. Li, J. Deng and F. Chen, Progress of graphite carbon nitride with different dimensions in the photocatalytic degradation of dyes: a review, *J. Alloys Compd.*, 2022, **901**, 163589.

11 Y. Luo, C. Li, Z. Liu, W. Guo, C. Sun, S. Zhao, Q. Wang, Y. Li, L. Chen, H. Zheng and F. Li, Photocatalytic activation of peroxymonosulfate (PMS) by CNN@NH_2-MIL-101(Fe) Z-scheme heterojunction for phthalates degradation under visible light irradiation, *Chem. Eng. J.*, 2024, **481**, 148683.

12 J. Li, D. Wang, S. Zhao, R. Ma, J. Guo, Z. Li, D. Wang, Y. Xuan and L. Wang, Enhanced peroxymonosulfate activation by S-scheme AgI/Cu-$BiVO_4$ heterojunction for efficient photocatalytic organics degradation and microcystis aeruginosa inactivation: performance, interfacial engineering and mechanism insight, *Appl. Catal., B*, 2024, **351**, 124007.

13 Y. Wan, H. Wang, J. Liu, X. Liu, X. Song, W. Zhou, J. Zhang and P. Huo, Enhanced degradation of polyethylene terephthalate plastics by CdS/CeO_2 heterojunction photocatalyst activated peroxymonosulfate, *J. Hazard. Mater.*, 2023, **452**, 131375.

14 J. Yang, T. Xie, Y. Mei, J. Chen, H. Sun, S. Feng, Y. Zhang, Y. Zhao, J. Wang, X. Li, J. He and H. Chen, High-efficiency V-mediated Bi_2MoO_6 photocatalyst for PMS activation: modulation of energy band structure and enhancement of surface reaction, *Appl. Catal., B*, 2023, **339**, 123149.

15 Z. Huang, H. Yu, L. Wang, X. Liu, S. Ren and J. Liu, Ferrocene-modified Uio-66-NH_2 hybrids with g-C_3N_4 as enhanced photocatalysts for degradation of bisphenol a under visible light, *J. Hazard. Mater.*, 2022, **436**, 129052.

16 J. Li, T. Sun, Y. Deng, H. Liu, R. Guan, C. Li, F. Zeng, T. Sun and C. Liu, Construction of photocatalytic-persulfate synergistic system for efficient removal of environmental pollutants, *Sep. Purif. Technol.*, 2025, **360**, 131033.

17 R. Chen, H. Zhang, Y. Dong and H. Shi, Dual metal ions/BNQDs boost PMS activation over copper tungstate photocatalyst for antibiotic removal: Intermediate, toxicity assessment and mechanism, *J. Mater. Sci. Technol.*, 2024, **170**, 11.

18 H. Yang, X. Cao, Y. He, X. Zhang, P. Zhang, X. Wang, Y. Liu, S. Xu, Y. Fang and L. Gu, Fe, N-CQDs triggered the fabrication of alginate encapsulated g-C_3N_4 hydrogel for efficient photocatalytic activation of PMS and antibiotic degradation, *Carbohydr. Polym.*, 2025, **351**, 123072.

19 S. Lv, X. Wang, X. Wei, Y. Zhang, Y. Cong and L. Che, Introduction of cluster-to-metal charge transfer in UiO-66-NH2 for enhancing photocatalytic degradation of bisphenol a in the existence of peroxymonosulfate, *Sep. Purif. Technol.*, 2022, **292**, 121018.

20 D. Guo, Y. Wang, C. Chen, J. He, M. Zhu, J. Chen and C. Zhang, A multi-structural carbon nitride co-modified by Co, S to dramatically enhance mineralization of bisphenol f in the photocatalysis-PMS oxidation coupling system, *Chem. Eng. J.*, 2021, **422**, 130035.

21 L. Yao, X. He, J. Lv, G. Xu, Z. Bao, J. Cui, D. Yu and Y. Wu, Efficient degradation of ciprofloxacin by Co_3O_4/Si nanoarrays heterojunction activated peroxymonosulfate under simulated sunlight: performance and mechanism, *J. Environ. Chem. Eng.*, 2022, **10**, 107397.

22 J. Wang, J. Yao, L. Yin, B. Wang, X. Liu, L. Yuan, C. Zhang, T. Bao, C. Liu and X. Hu, Facet engineering of metal-organic frameworks for efficient tetracycline degradation by

photocatalytic activation of peroxymonosulfate, *Chem. Eng. J.*, 2024, **497**, 154836.

23 X. Du, H. Du, B. Tang and C. Lai, Elaboration of a green and highly dispersible Co-MOFs induced Co-doped C_3N_5 photocatalyst: Applications and mechanistic insights into activated perxymonosulfate degradation of antibiotics, *J. Environ. Chem. Eng.*, 2024, **12**, 112186.

24 Y. Fan, W. Zhang, K. He, L. Wang, Q. Wang and J. Liu, Half-salen Fe(III) covalently post-modified MIL-125(Ti)-NH_2 MOF for effective photocatalytic peroxymonosulfate activation, *Appl. Surf. Sci.*, 2022, **591**, 153115.

25 B. Chen, L. Liu, Y. Song, H. Liu, Z. Gong, Y. She, J. Liu, R. Niu and J. Gong, Functional upcycling of waste polyester into Cr-MOF towards synergistic interfacial solar evaporation and organic pollutant degradation, *Mater. Today Sustainability*, 2023, **24**, 100561.

26 Z. Qian, R. Zhang, Y. Xiao, H. Huang, Y. Sun, Y. Chen, T. Ma and X. Sun, Trace to the source: self-tuning of MOF photocatalysts, *Adv. Energy Mater.*, 2023, **13**, 2300086.

27 X. Deng, L. Yang, H. Huang, Y. Yang, S. Feng, M. Zeng, Q. Li and D. Xu, Shape-defined hollow structural Co-MOF-74 and metal nanoparticles@Co-MOF-74 composite through a transformation strategy for enhanced photocatalysis performance, *Small*, 2019, **15**, 1902287.

28 S. Ding, J. Wan, Y. Ma, Y. Wang, M. Pu, X. Li and J. Sun, Water stable SiO_2-coated Fe-MOF-74 for aqueous dimethyl phthalate degradation in PS activated medium, *J. Hazard. Mater.*, 2021, **411**, 125194.

29 S. Ding, J. Wan, Y. Ma, Y. Wang, X. Li, J. Sun and M. Pu, Targeted degradation of dimethyl phthalate by activating persulfate using molecularly imprinted Fe-MOF-74, *Chemosphere*, 2021, **270**, 128620.

30 T. Zhang, X. Sun, S. Weng, S. Zhang, C. Xu, X. Gao and N. Zhu, Enhancing photocatalytic performance of rose-shaped Co/Ni bimetallic organic framework for reducing CO_2 to CO under visible light, *J. Mol. Struct.*, 2025, **1321**, 140190.

31 I. Strauss, A. Mundstock, D. Hinrichs, R. Himstedt, A. Knebel, C. Reinhardt, D. Dorfs and J. Caro, The interaction of guest molecules with Co-MOF-74: a Vis/NIR and Raman approach, *Angew. Chem., Int. Ed.*, 2018, **57**, 7434.

32 Q. Qian, Y. Li, Y. Liu, L. Yu and G. Zhang, Ambient fast synthesis and active sites deciphering of hierarchical foam-like trimetal-organic framework nanostructures as a platform for highly effcient oxygen evolution electrocatalysis, *Adv. Mater.*, 2019, **31**, 1091139.

33 Y. Ouyang and Q. Yang, High-performance visible-light photocatalysts for H_2 production: rod-shaped Co_3O_4/CoO/Co_2P heterojunction derived from Co-MOF-74, *J. Colloid Interface Sci.*, 2023, **644**, 346.

34 J. Wang, W. Wang, J. Li, X. Mu, X. Yan, Z. Wang, J. Su, T. Lei and C. Wang, Universal strategy to prepare a flexible photothermal absorber based on hierarchical Fe-MOF-74 toward highly efficient solar interfacial seawater desalination, *ACS Appl. Mater. Interfaces*, 2021, **38**, 13.

35 Y. Wang and R. Yu, Investigation of the catalytic effect of defective Ni-MOF-74 on polymerization of dopamine and multi-pore polydopamine photothermal coating constructed with defective Ni-MOF-74 particles, *J. Environ. Chem. Eng.*, 2023, **11**, 110422.